RSC Advances

This article can be cited before page numbers have been issued, to do this please use: M. J. Hajipour, O. akhavan, A. Meidanchi, S. Laurent and M. Mahmoudi, *RSC Adv.*, 2014, DOI: 10.1039/C4RA10862K.

ROYAL SOCIETY OF CHEMISTRY

www.rsc.org/advances

View Article Online
DOI: 10.1039/C4RA10862K

Hyperthermia-induced protein corona improves the therapeutic effects of zinc ferrite spinel-graphene sheets against cancer

Mohammad Javad Hajipour,[a,b] Omid Akhavan,[*c] Alireza Meidanchi,[c,d] Sophie Laurent,[e] and Morteza Mahmoudi[*b,f,g]

[a]The Persian Gulf Marine Biotechnology Research Center, Bushehr University of Medical Sciences, Bushehr, Iran

[b]Department of Nanotechnology and Nanotechnology Research Center, Faculty of Pharmacy, Tehran University of Medical Sciences, Tehran, Iran,

[c]Department of Physics, Sharif University of Technology, P.O. Box 11155-9161, Tehran, Iran

[d]Department of Physics, Payame Noor University (PNU), P.O. Box 19395-3697, Tehran, Iran

[e]Department of General, Organic and Biomedical Chemistry, NMR and Molecular Imaging Laboratory, University of Mons, 19 Avenue Maistriau, B-7000 Mons, Belgium

[f]Department of Pediatrics, Division of Cardiology, Stanford University School of Medicine, Stanford, California, United States

[g]Division of Cardiovascular Medicine, Department of Medicine, Stanford University School of Medicine, Stanford, California, United States

Address correspondence to: (OK) email: oakhavan@sharif.edu; (MM) email: mahmoudi@stanford.edu

View Article Online
DOI: 10.1039/C4RA10862K

Abstract

Superparamagnetic zinc ferrite spinel-graphene nanostructures were synthesized as potentially therapeutic agents in the magnetic targeted photothermal therapy of cancer and/or drug delivery. The global temperature of the solution and the local temperature at the nanoparticle (NP) surface determine the protein corona composition/content, which in turn affects the biological effects of NPs and the corresponding physiological responses. Therefore, it is rational to hypothesize that spinel-graphene nanostructures may have distinct protein corona compositions and contents, and therapeutic and toxic effects under laser irradiation. To assess this hypothesis, the effects of laser irradiation on the competitive binding of proteins to the spinel-graphene surface and the corresponding therapeutic effects of corona-coated spinel-graphene nanomaterials against cancer were evaluated. The results showed that the composition and content of the protein corona adsorbed onto the spinel-graphene nanomaterials was correlated with the local and global heating caused by laser irradiation. Moreover, the corona-coated spinel-graphene nanomaterials obtained following laser irradiation induced a higher intracellular concentration of reactive oxygen species (ROS) and exhibited a significantly higher cellular uptake efficacy compared to that achieved in the absence of laser irradiation (37ºC). This finding indicates that the therapeutic effects of graphene-based photothermal therapy against cancer are, in part, related to the composition and content of the protein corona formed under laser irradiation. The results of this study reveal that changes in the composition and content of the protein corona that occur during laser irradiation affect the therapeutic and toxic effects of NPs.

View Article Online
DOI: 10.1039/C4RA10862K

Introduction

Due to its unique chemical and physical properties, graphene (a two-dimensional sheet of sp^2-hybridized carbon atoms packed into a honeycomb lattice) is recognized as a rising star among the most promising nanomaterials used in various medical applications[1-5]. To develop suitable drug carriers, graphene is first oxidized to form a water-soluble graphene oxide (GO) derivative; it is then functionalized with various biocompatible and biostable molecules (*e.g.,* ethylene glycol) to increase its stability in biological media and decrease the risk of the potential toxicity of graphene in living organisms[6-8]. In recent years, graphene-based photothermal therapy has emerged as a promising approach to ablate cancer cells at high temperature under laser irradiation[7, 9]. However, the detailed mechanisms of graphene-based photothermal cancer ablation must be understood to maximize the therapeutic efficacy and minimize the side effects of this approach. Upon the immersion of nanoscale materials (including GO sheets) in a biological medium, the surfaces of the materials are covered by various types of biomolecules (forming a so-called "protein corona")[10-13]. Thus, the type and amount of the associated proteins in the protein corona defines the biological fate of nanoscale objects[14, 15]. Therefore, cancer and normal cells perceive this new, biologically modified structure of NPs formed in physiological media[16]. The formation of a protein corona is dependent on several parameters, such as the physicochemical properties of NPs[17, 18], temperature and time of incubation[19-21] , the local temperature at the surface of NPs submitted to photoinduced heating[22], personalized plasma changes resulting in personalized protein coronas[23] and the concentration and source of plasma proteins[24-26]. Recently, we showed that slight temperature changes affect the binding of proteins to NP surfaces, which in turn affect the cellular internalization and cytotoxic effects of NPs[20, 21]. Because plasma proteins show high susceptibility to temperature fluctuations, it is reasonable that the global solution temperature determines the affinity of plasma proteins to NP surfaces. On the other hand, locally heated areas exhibiting higher temperatures at the surface of laser-activated NPs alter the protein corona in terms of the content of bound proteins and composition[22]. Taken together, our previous studies showed that the local and

View Article Online
DOI: 10.1039/C4RA10862K

global temperatures of irradiated NPs and their dispersing solution at which the protein corona is formed determine the protein composition and content of the corona. Although many studies on graphene-based photothermal cancer ablation have been performed[3, 9, 27-29], there is no information regarding the effects of hyperthermia-induced protein corona on the killing of cancer cells. In this work, zinc ferrite spinel-graphene ($ZnFe_2O_4$-rGO) nanomaterials with the capacity for laser activation (due in particular to their graphene component and an excellent response to external magnetic fields were synthesized[30, 31]. The effect of local heating (induced by laser irradiation) on the composition and content of the protein corona formed on the nanomaterials was studied using 1D-SDS-PAGE and Image J software. A comprehensive range of experimental approaches (*e.g.,* MTT, ROS and lysosome labeling assays) was then employed to evaluate the cancer-ablating ability of hyperthermia-induced protein coronas.

Results and discussion

Morphological study

The morphologies of the prepared GO and the $ZnFe_2O_4$-rGO were investigated by TEM and SEM, as shown in Figures 1a–1d (TEM and SEM images of the pure $ZnFe_2O_4$ nanoparticles are provided in Figure S1 of supporting information (SI)). TEM images of the GO sheets and the $ZnFe_2O_4$ nanoparticles (with dimensions of ~5-10 nm) attached to one of the rGO sheets are presented in Figures 1a and 1b. SEM images of the GO sheets and $ZnFe_2O_4$-rGO nanomaterial powders are also shown in Figures 1c and 1d. It can be observed that the lateral size of the sheets was ~0.2–2 μm and that the $ZnFe_2O_4$ nanoparticles were uniformly deposited on the graphene sheets (as templates of the nanoparticles).

To better characterize the topography of the $ZnFe_2O_4$-rGO sheets, AFM was utilized. AFM image (e) shows two partially overlapped graphene sheets covered by nanoparticles with an average size of 20 nm. The height profile diagram of the AFM image (f) exhibits sharp peaks with a height of ~5 nm, which is consistent with the presence of $ZnFe_2O_4$ nanoparticles on the surface of the

View Article Online
DOI: 10.1039/C4RA10862K

graphene sheets. The height profile obtained from the edge of one of the sheets (g) indicates that the thickness of the sheets was ~0.7 nm, in good agreement with the typical thickness of a single-layer graphene oxide sheet (~0.8 nm). In fact, the typical thickness of a graphene oxide sheet is ~0.44 nm thicker than that of graphene (~0.36 nm) due to the presence of epoxy and/or hydroxyl groups on both sides of the oxide sheet[32-34]. As a benchmark for better comparison, AFM and SEM images of single-layer GO sheets can be found elsewhere[35-37].

View Article Online
DOI: 10.1039/C4RA10862K

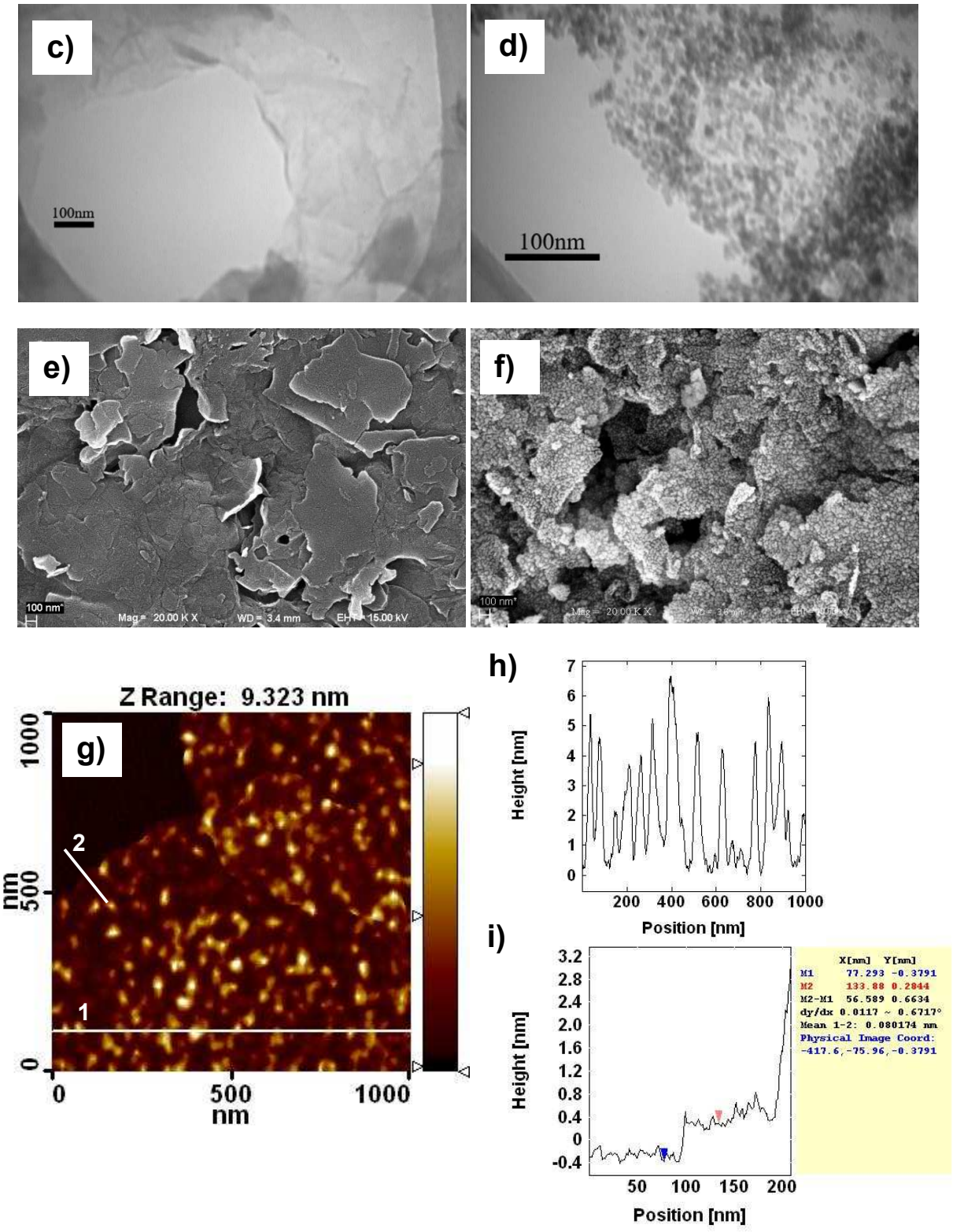

Fig. 1 TEM (a and b) and SEM (c and d) images of GO sheet (a and c) and $ZnFe_2O_4$-rGO composite (b and d) powders, e) AFM image of $ZnFe_2O_4$-rGO sheets deposited on a Si(111) substrate, and f) and g) height profile diagrams of the lines "1" and "2" shown in (e).

View Article Online
DOI: 10.1039/C4RA10862K

XRF Spectroscopy

Elemental analysis (Zn and Fe content) of $ZnFe_2O_4$ nanoparticles and $ZnFe_2O_4$-*GO* nanocomposite was determined by XRF Spectroscopy. The result of XRF is shown in Table 1. The Fe2O3/ZnO weight ratio was found ~3, indicating excess Fe_2O_3 in the composite (as compared to the weight ratio of ~2 for $ZnFe_2O_4$ composite). However, it should be noted that the obtained weight ratio was identical for $ZnFe_2O_4$ nanoparticles and $ZnFe_2O_4$-*GO* nanocomposite (i.e., independent from the incorporation of graphene in the composite).

Table 1. XRF results of nanomaterials (wt%)

	Fe_2O_3 (wt%)	ZnO (wt (%)
$ZnFe_2O_4$	75.30	24.69
$ZnFe_2O_4$-*GO*	75.51	24.48

Optical, chemical, structural and magnetic properties

Fig. 2A presents optical absorption spectra of the GO, $ZnFe_2O_4$ and $ZnFe_2O_4$-rGO suspensions. The hydrothermal reaction induced during the synthesis of the $ZnFe_2O_4$-rGO caused the color of the suspension to change from light brown (similar to color of the GO suspension) to black for the $ZnFe_2O_4$-rGO, as shown in the inset of **Fig. 2**A. The black color can be attributed to the partial restoration of the π network between the reduced sheets, resulting in electronic conjugation within the sheet[38]. Accordingly, the optical absorption spectrum of the GO suspension shows an absorption peak at approximately 231 nm, whereas in that for the $ZnFe_2O_4$-rGO suspension the absorption peak is shifted to a higher wavelength of approximately 375 nm. Similar optical spectra were previously reported for ZnO-GO and ZnO-rGO suspensions[39].

View Article Online
DOI: 10.1039/C4RA10862K

FTIR spectra of the GO, the $ZnFe_2O_4$, and the $ZnFe_2O_4$-rGO composite are shown in **Fig. 2**B. The absorption bands of the GO (**Fig. 2**Ba) are located at 3434 cm^{-1} (O–H stretching band), 1732 cm^{-1} (stretching band of C=O), 1628 cm^{-1} (skeletal vibrations of aromatic domains), 1398 cm^{-1} (bending absorption of carboxyl group O=C–O), 1230 cm^{-1} (O–H bending vibrations), and 1030 cm^{-1} (C–O stretching vibrations)[40]. A comparison of Figures 2Bb and 2Bc reveals that the main distinct bands are related to the presence of metal-oxygen stretching vibrations (Fe–O and Zn–O modes); that is, the bands located at 446 and 550 cm^{-1} appeared in the FTIR spectrum of the $ZnFe_2O_4$-rGO material, indicating the formation of a graphene-metal oxide composite[41]. Moreover, a comparison of Figures 2Ba and 2Bc indicates that the GO sheets in the graphene-metal oxide composite were effectively reduced through the hydrothermal reaction.

Raman spectroscopy is one of the most effective methods for investigating the carbon structure as well as the single- and multi-layer properties of graphene sheets. The G band (~1585 cm^{-1}), which is a well-known property of carbon-based materials, in the Raman spectra originates from the phonon scattering of the graphitic structure, and the D band (~1350 cm^{-1}), which is related to sp^3 defect bonds, may be caused by oxidation. Moreover, vacancies, grain boundaries, edge defects and amorphous carbon species in a disordered carbon structure can result in the formation of a D band. The I_G/I_D ratio is a well-known parameter for measuring the sp^2 domain size of a carbon structure containing sp^3 and sp^2 bonds. The I_D/I_G ratios for the GO and the $ZnFe_2O_4$-rGO materials were determined to be 1.53 and 1.25, respectively (see **Fig. 2**C). In fact, the deoxygenation of the GO sheets during the hydrothermal reaction may have resulted in the recovery of the graphitic structure of the sheets.

It is well known that the 2D band of the Raman spectra of carbon materials is highly sensitive to the stacking of graphene sheets[42]. For example, the 2D band of single-layer graphene is located at ~2679 cm^{-1}, whereas that for multi-layer graphene (2–4 layers) appears as a broader peak with a ~19 cm^{-1} shift toward higher wavenumbers[43]. Moreover, the I_{2D}/I_G ratios of single-, double-, triple- and multi- (> 4) layer graphene are > 1.6, ~0.8, ~0.30 and ~0.07, respectively[44-46]. In this

View Article Online
DOI: 10.1039/C4RA10862K

work, the I_{2D}/I_G ratios were determined to be 0.65 and 0.43 for the GO sheets and the $ZnFe_2O_4$-rGO composite, respectively. The decrease in the I_{2D}/I_G ratio can be attributed to the presence of aggregated sheets (formed during hydrothermal reduction) in the composite. These results confirmed the presence of graphene sheets (in the form of both single- and multi-layers) in the $ZnFe_2O_4$-rGO composite.

Over the range of 100–1000 cm^{-1}, $ZnFe_2O_4$ has a spinel structure with the symmetry of the Fd3m space group and has five active Raman modes ($A_{1g}+E_g+3F_{2g}$). **Fig. 2**C shows the five Raman modes at 217, 282, 396, 485 and 603 cm^{-1}. It is generally accepted that the modes above 600 cm^{-1} are of the A_{1g} type, involving motions of the O in tetrahedral AO_4 groups. Hence, the mode at 603 cm^{-1} could be assigned A_{1g} symmetry. The Raman spectra of the $ZnFe_2O_4$-rGO and the pure $ZnFe_2O_4$ materials showed similar features in the range of 100–1000 cm^{-1}, confirming the presence of $ZnFe_2O_4$ nanoparticles on the graphene sheets.

The magnetic properties of the $ZnFe_2O_4$ nanoparticles and the $ZnFe_2O_4$-rGO composite were studied using VSM. **Fig. 2**D shows the magnetization hysteresis loops of the samples. The saturated magnetization of the $ZnFe_2O_4$ and the $ZnFe_2O_4$-rGO were nearly 10 and 3.1 emu/g, respectively, at room temperature. Furthermore, we examined the magnetic properties of the $ZnFe_2O_4$-rGO suspension using a magnet, which caused the separation of the magnetic composite from the solution, as shown in the inset of **Fig. 2**D. It should be noted that the magnetism of graphene particles is a crucial requirement for the *in vivo* collection of nanomaterials via a strong external magnetic field.

View Article Online
DOI: 10.1039/C4RA10862K

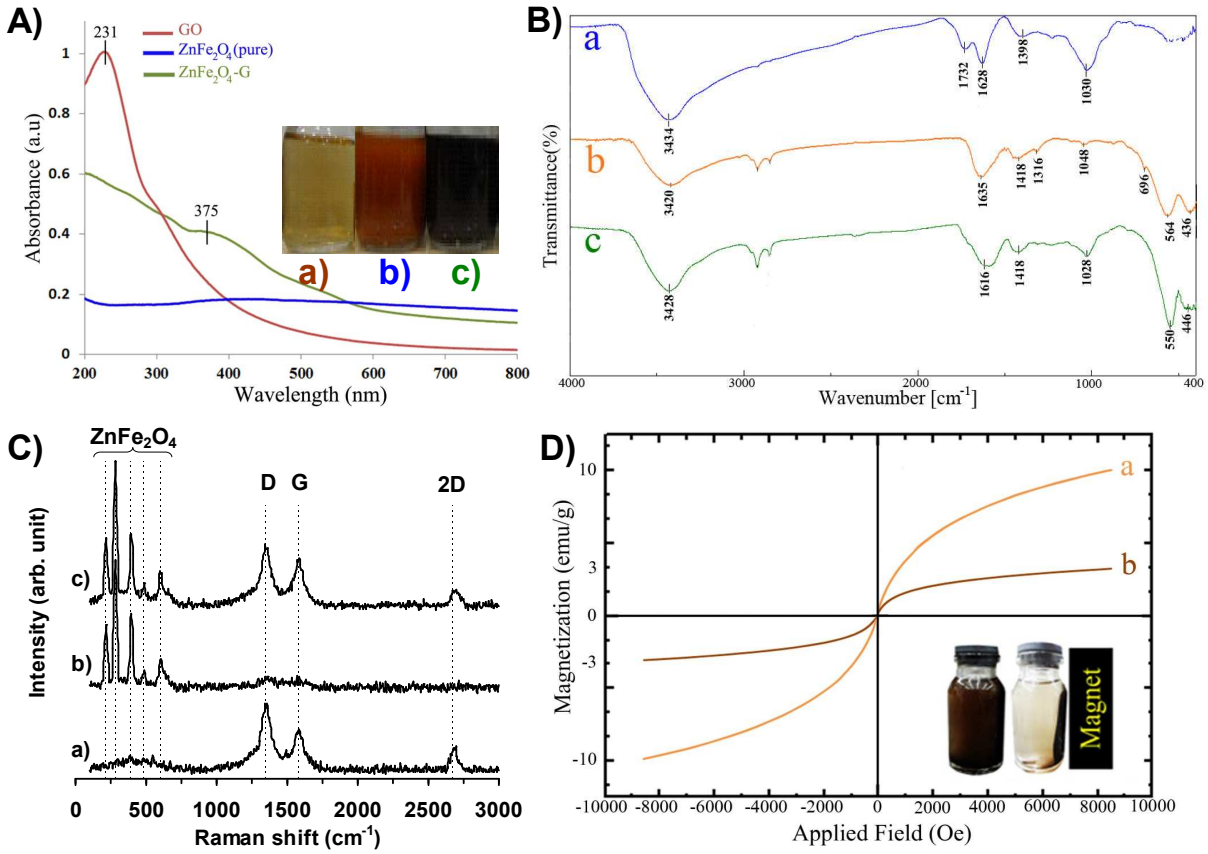

Fig. 2 A) UV-vis absorption spectra and digital image of a) GO, b) $ZnFe_2O_4$, and c) $ZnFe_2O_4$-rGO suspensions with GO concentration of 0.1 mg mL^{-1}; B) FTIR and C) Raman spectra of a) GO, b) $ZnFe_2O_4$ and c) $ZnFe_2O_4$-rGO composite; and D) magnetization hysteresis loops of a) $ZnFe_2O_4$ nanoparticles and b) $ZnFe_2O_4$-rGO composite. The inset of (D) shows the separation of the ZnFe2O4-rGO magnetic nanomaterials from their solution (ethanol) using a magnet.

Effects of laser irradiation on protein composition of coronas

To study the effect of photoinduced local heating on the composition of the hard protein corona of the nanomaterials, the materials were incubated with human plasma (50%) under continuous laser irradiation and their protein corona compositions were probed using 1D-SDS-PAGE. As shown in **Fig. 3**, the protein corona pattern induced in the laser-irradiated nanomaterials was different from that of the non-irradiated nanomaterials. For example, two protein bands at ~80 kDa and ~190 kDa clearly appeared in the hard corona of the laser-irradiated nanomaterials, whereas two distinct protein bands at ~60 kDa and ~90 kDa appeared in the hard corona of the non-irradiated materials.

View Article Online
DOI: 10.1039/C4RA10862K

Certain protein bands appeared in the hard corona of both the irradiated and non-irradiated nanomaterials. This finding is in agreement with the results of our recent study demonstrating that photoinduced heating of NPs affects the protein composition and content of coronas[22]. It is well understood that during laser irradiation, the local temperature at the NP surface is significantly higher than the global temperature of the dispersing solution[47, 48]. Therefore, it can be suggested that the higher local temperature at the surface of laser-activated NPs may result in significant protein conformational changes, which in turn affect the proteins' adsorption to the surface of NPs. On the other hand, laser irradiation increased the incubation temperature by elevating the global temperature of the dispersing solution, leading to conformational changes in the proteins depending on their distance from the NPs. Indeed, the conformational changes of plasma proteins that occur during photoinduced heating may affect the protein-NP and protein-protein interactions that in turn determine the composition and content of protein coronas. Therefore, one can expect that the plasma proteins submitted to photoinduced heating may have exhibited different affinities and accessibilities to NPs compared to those that were not exposed to laser irradiation.

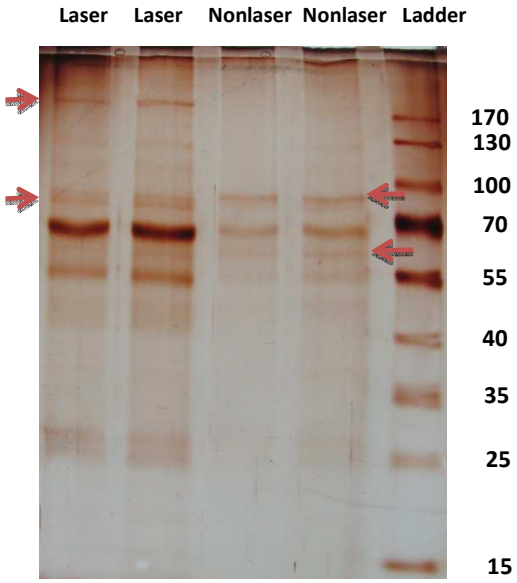

Fig. 3 SDS-PAGE (15% polyacrylamide) results for laser-irradiated and non-irradiated corona-coated $ZnFe_2O_4$-rGO obtained following incubation with 50% human plasma (Mass (kDa)).

View Article Online
DOI: 10.1039/C4RA10862K

Effects of laser irradiation on protein content of coronas

Because the protein content of coronas determines the biological effects of NPs[19], we measured the concentration of proteins bound to the surface of NPs using ImageJ software. In this respect, the intensities of three categories of proteins with different molecular weights (>100 kDa, 100-40 kDa and <40 kDa) were measured. As shown in **Fig. 4**, the intensity of the proteins associated in the hard corona of nanomaterials exposed to laser irradiation was significantly higher than that of materials that were incubated under physiological conditions (37 °C). This finding suggests that the higher local and/or global temperature induced during laser irradiation led to significant protein conformational changes, which in turn affected their affinity to the surface of NPs. This finding demonstrates that laser irradiation not only affected the corona composition but also affected the content of proteins bound to the surface of NPs.

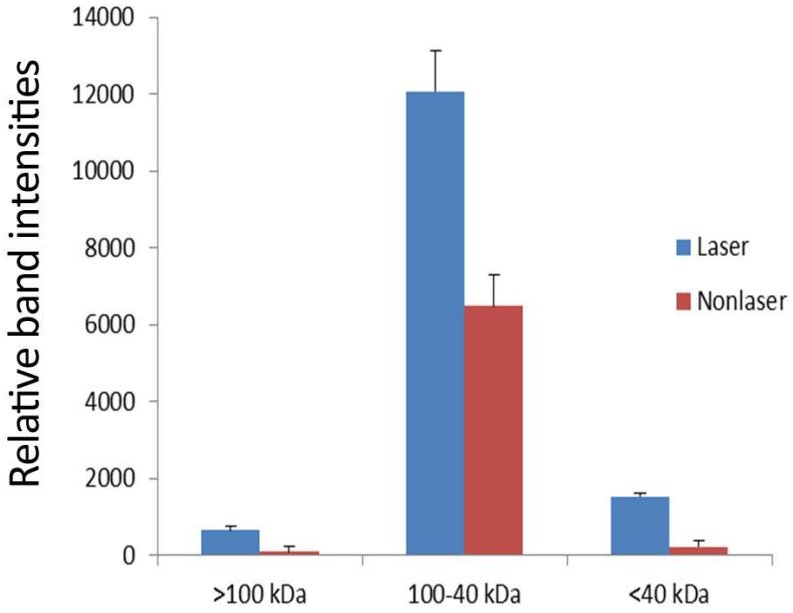

Fig. 4 Relative intensity of proteins associated within the laser-irradiated and non-irradiated corona-coated $ZnFe_2O_4$-rGO composites obtained following incubation with 50% human plasma.

View Article Online
DOI: 10.1039/C4RA10862K

To date, scientists have focused on the therapeutic and toxic effects of the physicochemical properties of NPs. Because the protein composition and content of coronas determines the biological fate of NPs and the corresponding physiological responses, it is reasonable to hypothesize that the changes in corona composition and content that occur during laser irradiation may affect the therapeutic impacts of NPs against cancer. To validate this hypothesis, the therapeutic effects of laser-irradiated corona-$ZnFe_2O_4$-rGO complexes against cancer were evaluated using different approaches such as MTT, ROS and lysosome labeling assay.

Cytotoxic effects of laser-irradiation-induced corona-$ZnFe_2O_4$-rGO complex

The cytotoxic effects of laser-irradiated and non-irradiated corona-$ZnFe_2O_4$-rGO complexes on MDA-MB-231 cells were investigated using the MTT assay, the results of which are shown in **Fig. 5**. The data obtained from the MTT assay showed that both the laser-irradiated and non-irradiated corona-$ZnFe_2O_4$-rGO complexes had similar cytotoxic effects on the MDA-MB-231 cells. This finding indicates that the corona composition and content of the corona-$ZnFe_2O_4$-rGO complexes provided no considerable contribution to the particles' cytotoxicity. Therefore, it can be concluded that the protein corona layer prevents the direct physical interaction of the nanomaterials with the cell membrane. This finding confirms the results of previous studies demonstrating that the cytotoxic effect of graphene and its derivatives is mainly attributed to their direct physical interaction with the cell membrane leading to irreversible cell damage[49, 50]. Therefore, it can be expected that disruption or damage of the cell membrane occurred as a result of the photoinduced heating of cancer cells by laser irradiation.

View Article Online
DOI: 10.1039/C4RA10862K

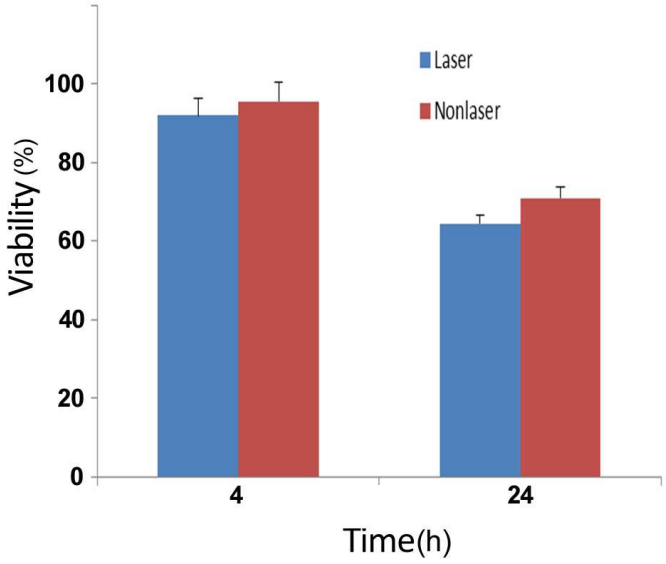

Fig. 5 Cell viability of MDA-MB-231 cells incubated with laser-irradiated and non-irradiated corona-coated $ZnFe_2O_4$-rGO composites for 4 and 24 hours.

ROS produced by hyperthermia-induced corona $ZnFe_2O_4$-rGO complex

Oxidative stress, which refers to the imbalance between destructive oxidants (ROS) and defensive antioxidants, results in significant cellular damage via induction of genotoxicity, inflammation and damage to critical biomolecules such as DNA, proteins and lipids[51-53]. It is well known that a regulated concentration of ROS is crucial for cancer cell proliferation, whereas the excessive production or reduction of ROS results in apoptosis and cell death. Therefore, disturbing ROS hemostasis can be as promising approach to killing cancer cells. Because cancer cells exhibit higher ROS levels than normal cells do[53], increasing these levels furthers offers an extraordinary opportunity for inducing damage to cancer cells. To study the effects of hyperthermia-induced corona formation on the ROS hemostasis of cancer cells, laser-irradiated and non-irradiated corona-$ZnFe_2O_4$-rGO complexes were incubated with MDA-MB-231 cells and the level of ROS production was evaluated using the H2 DCFDA assay. As shown in **Fig. 6**, the laser-irradiated corona-$ZnFe_2O_4$-rGO complexes induced a significantly higher level of ROS compared to that induced by the non-irradiated complexes. Indeed, different corona compositions and contents resulted in the generation of different ROS components and ROS concentrations. This finding indicates that the

View Article Online
DOI: 10.1039/C4RA10862K

corona composition and content formed in the presence of laser irradiation contributed to ROS generation. Therefore, the disturbance of ROS hemostasis that occurred during laser irradiation is, in part, related to the corona composition and content. In a previous study, Minai et al.[54] demonstrated that laser pulse irradiation increases ROS generation in gold NP targeted breast cancer cells. The authors speculated that laser irradiation damaged the cancer cells by inducing hyperthermia and ROS generation. Our findings demonstrate that the protein corona formed during laser irradiation act synergistically with laser irradiation and the corresponding hyperthermia induced, significantly promoting ROS generation mediating damage to cancer cells.

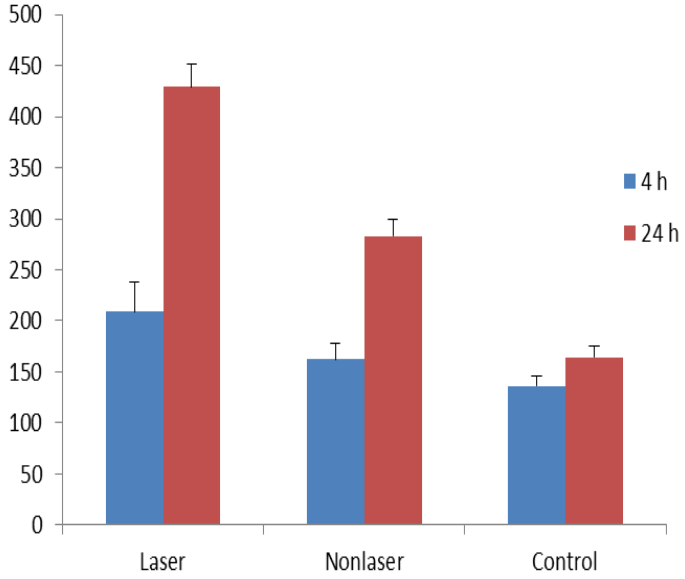

Fig. 6 The level of ROS production in MDA-MB-231 cells incubated with laser-irradiated and non-irradiated corona-coated $ZnFe_2O_4$-rGO composites for 4 and 24 hours.

Cellular uptake of hyperthermia-induced corona-coated $ZnFe_2O_4$-rGO

It is well accepted that the cytotoxic effect of NPs is strongly dependent on the particles' cellular uptake efficacy[55]. Indeed, NPs generally exert their therapeutic and toxic effects during and following cellular internalization. The physicochemical properties of NPs and the protein composition and content of coronas affect the cellular uptake and intracellular pathway of NPs[56-59].

View Article Online
DOI: 10.1039/C4RA10862K

The cellular internalization of graphene sheets mainly occurs through membrane diffusion at corner sites and edge asperities[60]. It is well understood that after cellular uptake, corona-coated graphene nanomaterials ultimately reside in the lysosome compartment[61]. Therefore, due to their high tendency to reside in lysosomes, LysoTracker analysis can serve as the best method for evaluating the intracellular concentration of corona-coated graphene. As shown in **Fig. 7**, the uptake level of the laser-irradiated corona-$ZnFe_2O_4$-rGO complexes was significantly higher than that of the non-irradiated complexes. This finding indicates that hyperthermia-induced protein corona formation enhances the cellular uptake of corona-$ZnFe_2O_4$-rGO complexes. This result is in agreement with previous studies showing that the corona composition and content affect the cellular uptake of NPs[19, 21]. Therefore, in addition to photothermal cell damage, higher cellular uptake occurs during laser irradiation, which indicates that hyperthermia-induced protein coronas have synergic effects with hyperthermia and laser irradiation, mediates cancer cell damage. During laser irradiation, cancer cells can be killed as a result of the heat generated and the protein corona composition and content induced by laser irradiation.

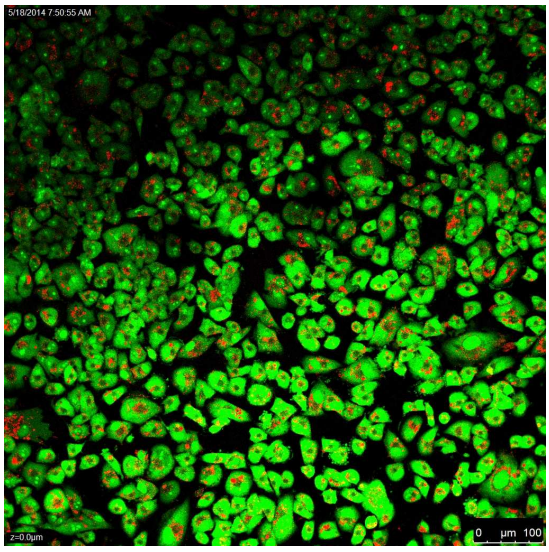

(A)

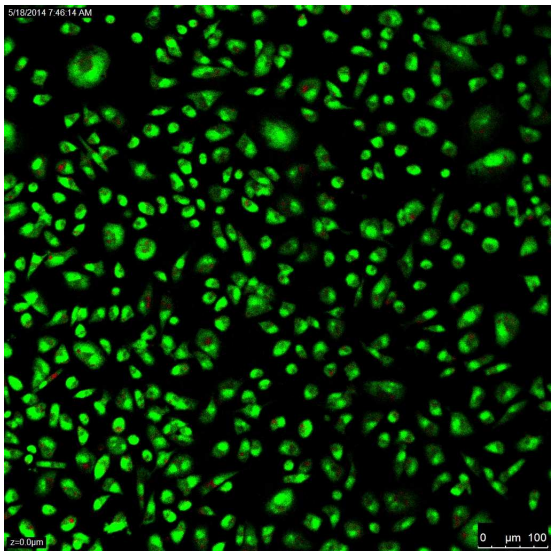

(B)

View Article Online
DOI: 10.1039/C4RA10862K

Fig. 7 Lysosome induction in MDA-MB-231 cells incubated with A) laser-irradiated and B) non-irradiated corona-coated $ZnFe_2O_4$-rGO for 2 hours. The lysosomes and cells were visualized using red and green fluorescent dyes, respectively.

Conclusion

In contrast to the current view that assumes that the cancer-ablating ability of graphene-based photothermal therapy is attributed only to the local heating of cancer cells, this research reveals that the therapeutic effects of graphene-based photothermal therapy against cancer are, in part, related to the protein composition and content of the coronas formed under continuous laser irradiation. Indeed, hyperthermia-induced protein corona formation was observed to improve the therapeutic effects of laser-activated nanomaterials against cancer. It is concluded that laser-irradiation-induced protein corona formation should be considered in future studies to gain a deep understanding of the detailed mechanism underlying photothermal therapy.

Experimental

Reagents

Natural graphite powder (purity ≥99.0%, particle size of ≤20 μm) and $KMnO_4$ were obtained from Fluka. Other products ($NaNO_3$, $Zn(NO_3)_2 \cdot 6H_2O$, and $Fe(NO_3)_3 \cdot 9H_2O$) were purchased from Sigma-Aldrich and used as received.

Synthesis of graphite oxide

Graphite oxide was synthesized using a modified version of the method originally developed by Hummers and Offeman[62]. First, we mixed 1.0 g graphite and 1.0 g $NaNO_3$ with 46 mL H_2SO_4 in an ice bath (0–5°C) and stirred the mixture for 15 min. Then, 6.0 g $KMnO_4$ was slowly added to the suspension such that temperature of the suspension was controlled to be less than 20°C. The

View Article Online
DOI: 10.1039/C4RA10862K

suspension was then stirred continuously in a water bath for 2 h at 35°C. Subsequently, the suspension was diluted by adding 80 mL deionized (DI) water; the temperature of the suspension was slowly increased to 98°C and maintained at that temperature for 15 min. Finally, 200 mL DI water and 6.0 mL H_2O_2 (30%) were added to the mixture to terminate the reaction. The acquired mixture was filtered (Schleicher and Schuell membrane filters measuring 120 mm in diameter and 0.2 μm in pore size) and washed with HCl (5%) and DI water (the latter for three times). Then, the graphite oxide suspension (obtained through redispersion of the filtered material in DI water) was centrifuged at 2000 rpm for 15 min. Finally, the material remaining in the centrifuge tube was dried at 60°C for 12 h to obtain graphite oxide powder.

Synthesis of $ZnFe_2O_4$-rGO nanomaterial

$ZnFe_2O_4$-rGO containing 20 wt% graphene was synthesized by coprecipitation of $Zn(NO_3)_2{\cdot}6H_2O$ and $Fe(NO_3)_3{\cdot}9H_2O$ in the presence of GO. To this end, 30 mg graphite oxide dispersed in 60 mL ethanol was sonicated at a frequency of 40 kHz and power of 100 W for 60 min. Then, 150 mg $Zn(NO_3)_2{\cdot}6H_2O$ and 400 mg $Fe(NO_3)_3{\cdot}9H_2O$ were added to 20 mL ethanol, and the mixture was stirred for 30 min. The obtained solution was added to the GO suspension, and the mixture was stirred for 30 min. Then, the mixture was sealed in a Teflon-lined stainless steel autoclave and heated to 180°C for 12 h. The mixture obtained was left to cool at room temperature. The resulting black $ZnFe_2O_4$-rGO powder was rinsed with DI water several times and dried in an oven at 60°C for 24 h. Although GO can be reduced at high temperatures in a reducing or even inert atmosphere, and/or under alkaline conditions, in this study, the GO sheets were reduced by the hydrothermal reaction, as reported by other researchers[63]. In fact, the hydrothermal reaction not only results in an easy one-pot reaction for synthesizing a composite material but also efficiently reduces the GO sheets contained in the composite at the same time.

Material characterizations

View Article Online
DOI: 10.1039/C4RA10862K

The morphologies of the GO sheets and the $ZnFe_2O_4$-rGO nanomaterials were characterized using a Hitachi S-4200 scanning electron microscope (SEM) at an accelerating voltage of 15 kV and a Zeiss-EM10C transmission electron microscope (TEM) at an accelerating voltage of 80 kV. The TEM samples were prepared by dipping carbon-coated copper grids into an acetone solution containing the powder of the synthesized material. The surface topography and height profile of the $ZnFe_2O_4$-rGO sheets were further investigated by atomic force microscopy (AFM, Park Scientific model CP-Research, VEECO) in tapping mode. Optical absorption spectra of the samples were recorded using a UV-visible spectrophotometer (CARY 300 Conc) over the wavelength range of 200–800 nm. Fourier transform infrared (FTIR) spectra were recorded by using a FTIR-4200 JASCO equipped with pressed KBr pellets over the wavenumber range of 400 to 4000 cm^{-1}. Raman spectroscopy was performed at room temperature using a HR-800 Jobin-Yvon equipped with a 532 nm neodymium-doped yttrium-aluminum-garnet (Nd-YAG) excitation source to study the carbon structure of the graphene-based nanomaterials. The magnetic properties of the nanomaterials were examined by using a vibrating sample magnetometer (VSM/AGFM-Meghnatis Kavir Kashan Co.) with a maximum applied magnetic field of 10 kOe,

Preparation of hard-corona-coated ZnFe2O4-rGO nanomaterial

Because slight changes in temperature affect protein corona formation, the $ZnFe_2O_4$-rGO nanomaterials and human plasma were pre-incubated at 37ºC for 5 min. One hundred microliters of $ZnFe_2O_4$-rGO nanomaterial stock solution (1 mg/ml) were incubated with human plasma (500 µl of plasma + 400 µl of PBS) at a concentration of 50%. Following the initial incubation, the reaction mixtures were exposed to continuous laser irradiation (cw Nd:YVO4 laser, wavelength 405 nm, power 100 mW) and/or conventional physiological temperature (37°C) for 1 hour. At the end of the 1 hour period, the incubated samples were centrifuged at 18000 g for 30 min to pellet the nanomaterial-protein complexes. The pellet was then resuspended in 1000 µL of cold (15°C) phosphate buffer saline (PBS) and centrifuged again at 18000 g for 20 min (washing step). The

View Article Online
DOI: 10.1039/C4RA10862K

washing step was repeated three times to remove unbound and loosely bound proteins (soft corona). Finally, the corona-coated NP pellet was resuspended in PBS and used for different assays.

X-Ray Fluorescence (XRF) Spectroscopy

Semi quantitative elemental analysis of nanoparticles was determined by X-Ray Fluorescence Spectroscopy (XRF, link analytical, XR300, UK) with accuracy of ±1 ppm in vacuum conditions, tube voltage of 40 kV, tube current of 100 μA in 100s.

SDS-PAGE and densitometry analyses

The obtained corona-coated nanomaterials were mixed with protein loading buffer and boiled for 10 min at 100 ºC; then, an identical volume of each sample was loaded in 15% polyacrylamide gel. Gel electrophoresis was run at 120 V, 80 mA for 100 min, and the gels were stained with silver nitrate to observe the low-abundance-protein bands. A semi-quantitative densitometry analysis was conducted to quantify the intensity of associated proteins in the hard corona. The intensity of protein bands with different molecular weights (>100 kDa, 40-100 kDa and <40 kDa) was measured using Image J software (Version 1.410).

Cell culture and MTT assay

MDA-MB-231 cells (purchased from the national cell bank of Iran (NCBI)) were seeded in a 96-well plate, with approximately 10000 cells per well. The cells were cultured in 100 μL pyruvate-free DMEM culture medium supplemented with 10% fetal bovine serum (FBS) and antibiotic (100 μg/mL streptomycin and 100 U/mL penicillin) for 24 h at 37 ˚C in a 5% Co_2 incubator. After 24 hours, the DMEM media containing 10% FBS was replaced with FBS-free DMEM medium containing corona-coated $ZnFe_2O_4$-rGO nanomaterials (100 μg/ml) and incubated for an additional 4 and 24 hours at 37 ˚C. For control cells, the medium was replaced with FBS-free medium containing no nanomaterial. The cytotoxic effect of the corona-coated $ZnFe_2O_4$-rGO nanomaterials was evaluated using the 3-(4,5-dimethylthiazol-2yl)-2,5-diphenyltetrazolium bromide (MTT) assay.

View Article Online
DOI: 10.1039/C4RA10862K

To this end, 100 µl of MTT solution (0.5 mg/ml) was added to each well and maintained in the dark for 3 hours. Following incubation, the MTT solution was replaced with 100 µl of DMSO, and the absorbance of each well medium was read at 570 nm (microplate reader (Labsystem multiskan MS)).

Reactive oxygen species (ROS) assay

The level of ROS production induced by the corona-coated $ZnFe_2O_4$-rGO nanomaterials was measured using the 5-(and-6)-chloromethyl-2,7-dichloro-dihydrofluorescein diacetate acetyl ester (H2 DCFDA) assay. After incubation (4 and 24 hours) of the MDA-MB-231 cells with the corona-coated $ZnFe_2O_4$-rGO nanomaterials, the cells were washed with PBS and incubated with H2 DCFDA (10 mM) for 1 hour at 37 ºC (dark condition). The cells were then rinsed, and the fluorescence intensity of each sample was assessed using a spectrofluorometer. The data obtained from this analysis were reported in terms of relative fluorescence intensity.

Lysosome labeling

A lysosome labeling assay was used to measure the cellular uptake efficacy of the corona-coated $ZnFe_2O_4$-rGO nanomaterials. After 2 hours incubation of the MDA-MB-231 cells with the corona-coated $ZnFe_2O_4$-rGO (100 µg/ml), the cells were labeled with LysoTracker® Red DND-99 to stain the lysosomes (Image-iT™ LIVE lysosomal and nuclear labeling kit). Briefly, LysoTracker® Red DND-99 (10 nM) was added to each well and incubated for 1 hour at 37 ºC. In the next step, the cells were rinsed and incubated with acridine orange dye for 10 min. Then, the cells were washed, and the level of lysosome induction was evaluated using confocal microscopy (Leica, TCS SP5).

Acknowledgements. OA would like to thank the Research Council of Sharif University of Technology for the financial support of this work.

View Article Online
DOI: 10.1039/C4RA10862K

View Article Online
DOI: 10.1039/C4RA10862K

References

1. O. Akhavan and E. Ghaderi, *Acs Nano*, 2010, 4, 5731-5736.
2. O. Akhavan and E. Ghaderi, *Nanoscale*, 2013, 5, 10316-10326.
3. O. Akhavan and E. Ghaderi, *Small*, 2013, 9, 3593-3601.
4. H. Y. Mao, S. Laurent, W. Chen, O. Akhavan, M. Imani, A. A. Ashkarran and M. Mahmoudi, *Chemical reviews*, 2013, 113, 3407-3424.
5. S. M. AminaGhiasi, *Nanoscale*, 2012, 4, 7322-7325.
6. L. Feng, S. Zhang and Z. Liu, *Nanoscale*, 2011, 3, 1252-1257.
7. O. Akhavan, E. Ghaderi, H. Emamy and F. Akhavan, *Carbon*, 2013, 54, 419-431.
8. O. Akhavan, E. Ghaderi and A. Akhavan, *Biomaterials*, 2012, 33, 8017-8025.
9. O. Akhavan, E. Ghaderi and H. Emamy, *Journal of Materials Chemistry*, 2012, 22, 20626-20633.
10. A. E. Nel, L. Mädler, D. Velegol, T. Xia, E. M. Hoek, P. Somasundaran, F. Klaessig, V. Castranova and M. Thompson, *Nature materials*, 2009, 8, 543-557.
11. I. Lynch and K. A. Dawson, *Nano Today*, 2008, 3, 40-47.
12. M. Mahmoudi, I. Lynch, M. R. Ejtehadi, M. P. Monopoli, F. B. Bombelli and S. Laurent, *Chemical reviews*, 2011, 111, 5610-5637.
13. U. Sakulkhu, L. Maurizi, M. Mahmoudi, M. Motazacker, M. Vries, A. Gramoun, M.-G. O. Beuzelin, J.-P. Vallée, F. Rezaee and H. Hofmann, *Nanoscale*, 2014.
14. C. D. Walkey and W. C. Chan, *Chemical Society Reviews*, 2012, 41, 2780-2799.
15. M. P. Monopoli, C. Åberg, A. Salvati and K. A. Dawson, *Nature nanotechnology*, 2012, 7, 779-786.
16. D. Walczyk, F. B. Bombelli, M. P. Monopoli, I. Lynch and K. A. Dawson, *Journal of the American Chemical Society*, 2010, 132, 5761-5768.
17. M. Lundqvist, J. Stigler, G. Elia, I. Lynch, T. Cedervall and K. A. Dawson, *Proceedings of the National Academy of Sciences*, 2008, 105, 14265-14270.
18. S. Tenzer, D. Docter, S. Rosfa, A. Wlodarski, J. r. Kuharev, A. Rekik, S. K. Knauer, C. Bantz, T. Nawroth and C. Bier, *Acs Nano*, 2011, 5, 7155-7167.
19. S. Tenzer, D. Docter, J. Kuharev, A. Musyanovych, V. Fetz, R. Hecht, F. Schlenk, D. Fischer, K. Kiouptsi and C. Reinhardt, *Nature nanotechnology*, 2013, 8, 772-781.
20. M. Mahmoudi, A. M. Abdelmonem, S. Behzadi, J. H. Clement, S. Dutz, M. R. Ejtehadi, R. Hartmann, K. Kantner, U. Linne and P. Maffre, *Acs Nano*, 2013, 7, 6555-6562.
21. M. Mahmoudi, M. A. Shokrgozar and S. Behzadi, *Nanoscale*, 2013, 5, 3240-3244.
22. M. Mahmoudi, S. E. Lohse, C. J. Murphy, A. Fathizadeh, A. Montazeri and K. S. Suslick, *Nano letters*, 2013, 14, 6-12.
23. M. J. Hajipour, S. Laurent, A. Aghaie, F. Rezaee and M. Mahmoudi, *Biomaterials Science*, 2014.
24. M. P. Monopoli, D. Walczyk, A. Campbell, G. Elia, I. Lynch, F. Baldelli Bombelli and K. A. Dawson, *Journal of the American Chemical Society*, 2011, 133, 2525-2534.
25. M. Ghavami, S. Saffar, B. A. Emamy, A. Peirovi, M. A. Shokrgozar, V. Serpooshan and M. Mahmoudi, *Rsc Advances*, 2013, 3, 1119-1126.
26. S. Laurent, C. Burtea, C. Thirifays, F. Rezaee and M. Mahmoudi, *Journal of colloid and interface science*, 2013, 392, 431-445.
27. K. Yang, J. Wan, S. Zhang, B. Tian, Y. Zhang and Z. Liu, *Biomaterials*, 2012, 33, 2206-2214.
28. X. Ma, H. Tao, K. Yang, L. Feng, L. Cheng, X. Shi, Y. Li, L. Guo and Z. Liu, *Nano Research*, 2012, 5, 199-212.
29. W. Zhang, Z. Guo, D. Huang, Z. Liu, X. Guo and H. Zhong, *Biomaterials*, 2011, 32, 8555-8561.
30. O. Akhavan, A. Meidanchi, E. Ghaderi and S. Khoei, *Journal of Materials Chemistry B*, 2014, 2, 3306-3314.
31. A. Meidanchi and O. Akhavan, *Carbon*, 2014, 69, 230-238.
32. H. C. Schniepp, J.-L. Li, M. J. McAllister, H. Sai, M. Herrera-Alonso, D. H. Adamson, R. K. Prud'homme, R. Car, D. A. Saville and I. A. Aksay, *The Journal of Physical Chemistry B*, 2006, 110, 8535-8539.
33. M. J. McAllister, J.-L. Li, D. H. Adamson, H. C. Schniepp, A. A. Abdala, J. Liu, M. Herrera-Alonso, D. L. Milius, R. Car and R. K. Prud'homme, *Chemistry of Materials*, 2007, 19, 4396-4404.

View Article Online
DOI: 10.1039/C4RA10862K

34. O. Akhavan, *Carbon*, 2010, 48, 509-519.
35. O. Akhavan, *Acs Nano*, 2010, 4, 4174-4180.
36. O. Akhavan, M. Kalaee, Z. Alavi, S. Ghiasi and A. Esfandiar, *Carbon*, 2012, 50, 3015-3025.
37. O. Akhavan, M. Abdolahad, A. Esfandiar and M. Mohatashamifar, *The Journal of Physical Chemistry C*, 2010, 114, 12955-12959.
38. D. Li, M. B. Müller, S. Gilje, R. B. Kaner and G. G. Wallace, *Nature nanotechnology*, 2008, 3, 101-105.
39. O. Akhavan, *Carbon*, 2011, 49, 11-18.
40. S. Stankovich, R. D. Piner, S. T. Nguyen and R. S. Ruoff, *Carbon*, 2006, 44, 3342-3347.
41. Y. Li, R. Yi, A. Yan, L. Deng, K. Zhou and X. Liu, *Solid State Sciences*, 2009, 11, 1319-1324.
42. L. Malard, M. Pimenta, G. Dresselhaus and M. Dresselhaus, *Physics Reports*, 2009, 473, 51-87.
43. D. Graf, F. Molitor, K. Ensslin, C. Stampfer, A. Jungen, C. Hierold and L. Wirtz, *Nano letters*, 2007, 7, 238-242.
44. K. S. Kim, Y. Zhao, H. Jang, S. Y. Lee, J. M. Kim, K. S. Kim, J.-H. Ahn, P. Kim, J.-Y. Choi and B. H. Hong, *Nature*, 2009, 457, 706-710.
45. A. A. Balandin, S. Ghosh, W. Bao, I. Calizo, D. Teweldebrhan, F. Miao and C. N. Lau, *Nano letters*, 2008, 8, 902-907.
46. L. Liu, S. Ryu, M. R. Tomasik, E. Stolyarova, N. Jung, M. S. Hybertsen, M. L. Steigerwald, L. E. Brus and G. W. Flynn, *Nano letters*, 2008, 8, 1965-1970.
47. J. Huang, K. S. Jackson and C. J. Murphy, *Nano letters*, 2012, 12, 2982-2987.
48. H.-C. Huang, K. Rege and J. J. Heys, *Acs Nano*, 2010, 4, 2892-2900.
49. W. Hu, C. Peng, M. Lv, X. Li, Y. Zhang, N. Chen, C. Fan and Q. Huang, *Acs Nano*, 2011, 5, 3693-3700.
50. H. Mao, W. Chen, S. Laurent, C. Thirifays, C. Burtea, F. Rezaee and M. Mahmoudi, *Colloids and Surfaces B: Biointerfaces*, 2013, 109, 212-218.
51. J. Wang and J. Yi, *Cancer biology & therapy*, 2008, 7, 1875-1884.
52. R. Franco, O. Schoneveld, A. G. Georgakilas and M. I. Panayiotidis, *Cancer letters*, 2008, 266, 6-11.
53. T. Ozben, *Journal of pharmaceutical sciences*, 2007, 96, 2181-2196.
54. L. Minai, D. Yeheskely-Hayon and D. Yelin, *Scientific reports*, 2013, 3.
55. E. C. Cho, Q. Zhang and Y. Xia, *Nature nanotechnology*, 2011, 6, 385-391.
56. S. Dasgupta, T. Auth and G. Gompper, *Nano letters*, 2014, 14, 687-693.
57. H. Jin, D. A. Heller, R. Sharma and M. S. Strano, *Acs Nano*, 2009, 3, 149-158.
58. H. Herd, N. Daum, A. T. Jones, H. Huwer, H. Ghandehari and C.-M. Lehr, *Acs Nano*, 2013, 7, 1961-1973.
59. A. Lesniak, F. Fenaroli, M. P. Monopoli, C. Åberg, K. A. Dawson and A. Salvati, *Acs Nano*, 2012, 6, 5845-5857.
60. Y. Li, H. Yuan, A. von dem Bussche, M. Creighton, R. H. Hurt, A. B. Kane and H. Gao, *Proceedings of the National Academy of Sciences*, 2013, 110, 12295-12300.
61. Q. Mu, G. Su, L. Li, B. O. Gilbertson, L. H. Yu, Q. Zhang, Y.-P. Sun and B. Yan, *ACS applied materials & interfaces*, 2012, 4, 2259-2266.
62. W. S. Hummers Jr and R. E. Offeman, *Journal of the American Chemical Society*, 1958, 80, 1339-1339.
63. Y. Zhou, Q. Bao, L. A. L. Tang, Y. Zhong and K. P. Loh, *Chemistry of Materials*, 2009, 21, 2950-2956.

View Article Online
DOI: 10.1039/C4RA10862K

TOC